

# Robust and Nonrobust Aspects of Atlantic Meridional Overturning Circulation Variability and Mechanisms in the Community Earth System Model

GOKHAN DANABASOGLU, LAURA LANDRUM, STEPHEN G. YEAGER, AND PETER R. GENT

*National Center for Atmospheric Research, Boulder, Colorado*

(Manuscript received 10 January 2019, in final form 25 July 2019)

## ABSTRACT

Robust and nonrobust aspects of Atlantic meridional overturning circulation (AMOC) variability and mechanisms are analyzed in several 600-yr simulations with the Community Earth System Model. The simulations consist of a set of cases where a few loosely constrained ocean model parameter values are changed, a pair of cases where round-off level perturbations are applied to the initial atmospheric temperature field, and a millennium-scale integration. The time scales of variability differ among the cases with the dominant periods ranging from decadal to centennial. These dominant periods are not stationary in time, indicating that a robust characterization of AMOC temporal variability requires long, multimillennium-scale simulations. A robust aspect is that positive anomalies of the Labrador Sea (LS) upper-ocean density and boundary layer depth and the positive phase of the North Atlantic Oscillation lead AMOC strengthening by 2–3 years. Respective contributions of temperature and salinity to these density anomalies vary across the simulations, but in a majority of the cases temperature contributions dominate. Following an AMOC intensification, all cases show that advection of warm and salty waters into the LS region results in near-neutral density anomalies. Analysis of the LS heat budget indicates that temperature acts to increase density in all cases prior to an AMOC intensification, primarily due to losses by sensible and latent heat fluxes. The accompanying salt budget analysis reveals that the salt contribution to density anomalies varies across the cases, taking both positive and negative values.

## 1. Introduction

The Atlantic meridional overturning circulation (AMOC) represents a zonally integrated view of the oceanic circulation in the Atlantic basin, usually depicted in latitude–depth or latitude–density space. In both observations and models, AMOC is responsible for the vast majority of the mean heat transport in the North Atlantic, accounting for >90%<sup>1</sup> of the near-peak transport of 1.2–1.3 PW at 26.5°N (Johns et al. 2011; Msadek et al. 2013). As such, variations in AMOC transport impact the heat (and salt) content of the North Atlantic, including that of the subpolar regions (Danabasoglu 2008). Thus, while properties and variability of deep-water formation (DWF) in the northern

North Atlantic impact AMOC, in turn AMOC itself influences deep-water properties and variability. In addition, AMOC affects the spatial and temporal variability of sea surface temperatures (SST) with numerous studies linking the low-frequency fluctuations in North Atlantic SSTs to variability in AMOC [see Zhang et al. (2019), and references therein]. These SST fluctuations are referred to as Atlantic multidecadal variability (AMV), which is characterized by basin-scale warming or cooling of the North Atlantic in a horseshoe-like pattern with the largest anomalies in the subpolar regions and weaker anomalies in the tropical North Atlantic (e.g., Enfield et al. 2001). Observational and proxy records suggest a range of 40–70 years as dominant AMV time scales (e.g., Schlesinger and Ramankutty 1994; Delworth and Mann 2000). AMV, in turn, has been shown to have many regional and global climate impacts, including on temperature and precipitation over Europe, North America, and Asia; Atlantic hurricanes; Sahel and Brazilian rainfall; shifts in the intertropical convergence zone; and Arctic sea ice. We refer to recent articles by Buckley and Marshall (2016),

<sup>1</sup>Based on an overturning–gyre decomposition. Also see Xu et al. (2016) for a heat transport analysis of the entire North Atlantic that includes other decompositions.

*Corresponding author:* Gokhan Danabasoglu, gokhan@ucar.edu

Sutton et al. (2018), and Zhang et al. (2019) for very comprehensive syntheses and reviews of the current state of research on AMOC-AMV linkages and AMV climate impacts.

AMOC-related observational efforts have gained significant momentum over the last decade or so, with several transbasin and western boundary arrays in place (see Frajka-Williams et al. 2019). These measurements, especially if they are sustained, will provide much needed information to decipher the origins and characteristics of decadal to multidecadal variability in AMOC. Until such long and continuous observational datasets are available, models remain the primary tools for studying (multi-)decadal- and longer-time-scale variability and associated mechanisms. Unfortunately, models are inconsistent in their representations of the AMOC mean state and the amplitude and dominant time scales of AMOC variability, as well as the dominant variability mechanisms (e.g., Liu 2012; Buckley and Marshall 2016). In control simulations—usually run for preindustrial conditions—of various coupled models participating in the Coupled Model Intercomparison Project (CMIP), the characteristic time scales of AMOC variability ranges from on the order of 20 years (Msadek et al. 2010; Danabasoglu 2008) to 100 years (Jungclauss et al. 2005). In historical simulations from phase 5 of CMIP (CMIP5), the maximum transport of the time-mean AMOC<sup>2</sup> varies from about 10 to 30 Sv (1 Sv  $\equiv 10^6 \text{ m}^3 \text{ s}^{-1}$ ), with time scales of variability ranging from decadal to multidecadal with amplitudes spanning about 1–4 Sv (Zhang and Wang 2013; Xu et al. 2019). Even in hindcast ocean–sea ice simulations participating in the Coordinated Ocean-ice Reference Experiments phase II (CORE-II) effort, where models are forced with the same interannually varying atmospheric datasets, the maximum time-mean AMOC transport magnitudes are between 8 and 28 Sv, and the penetration depth of the North Atlantic Deep Water (NADW) varies substantially among the models (Danabasoglu et al. 2014). Nevertheless, these hindcast simulations show more consistent and robust multidecadal AMOC variability among themselves (Danabasoglu et al. 2016) than is found in historical simulations from CMIP5 (Xu et al. 2019). Perhaps more surprisingly, there are large discrepancies among ocean reanalysis products in their representations of AMOC, despite the use of the same observational datasets to constrain their respective data assimilation systems (Karspeck et al. 2017).

Differences in AMOC mean and variability properties are also evident across many long control simulations with various versions of the Community Climate System Model (CCSM). As shown in Bryan et al. (2006), both the maximum mean transport and the amplitude of AMOC variability exhibit strong resolution dependencies in CCSM3, both decreasing with coarser resolution. Furthermore, in the nominal 1° (T85  $\times$  1) CCSM3 version, a 300-yr-long very regular oscillatory regime with a period of 21 years is followed by a much weaker red noise–like irregular variability with a broad range of periods peaking at about 40 years (Danabasoglu 2008; Kwon and Frankignoul 2012). In CCSM4, AMOC shows a broad spectrum of low-frequency variability with statistically significant<sup>3</sup> peaks in the 50–200-yr range (Danabasoglu et al. 2012b). There are also sensitivities to representations of subgrid-scale processes. Specifically, the inclusion of an overflow parameterization in CCSM4 results in lower decadal and longer time scale variability in the mid- to high-latitude Atlantic (Yeager and Danabasoglu 2012). In the same model, parameterized meso- and submesoscale eddies contribute significantly to salinity anomalies that dominate Labrador Sea (LS) density changes, thus suggesting that details of parameterizations and parameter values can matter (Danabasoglu et al. 2012b).

Despite the differences summarized above both within multimodel and single-model (i.e., CCSM) frameworks, a majority of the studies identify the northern North Atlantic, and particularly models' DWF regions, as important areas linked to AMOC variability (e.g., Danabasoglu et al. 2012b; Delworth and Zeng 2016; Buckley and Marshall 2016). A prevailing proposed low-frequency variability mechanism involves long episodes of the positive phase of the North Atlantic Oscillation (NAO+) (e.g., Eden and Willebrand 2001; Bentsen et al. 2004; Biastoch et al. 2008; Danabasoglu 2008; Yeager and Danabasoglu 2014). Specifically, surface buoyancy flux anomalies associated with such persistent NAO+ periods contribute to positive upper-ocean density anomalies and subsequently to deeper mixed layers in models' DWF regions, mostly in the LS. After a delay of a few years AMOC intensifies. Stronger AMOC then leads to increased northward heat transport a few years later, resulting in a convergence of heat (increased heat content) in the subpolar North Atlantic. Starting with the subpolar warming of the upper-ocean, basin-scale SST anomalies resembling that of AMV emerge. In some models, the resulting

<sup>2</sup> These transports represent the maximum magnitude of the North Atlantic Deep Water (NADW) cell.

<sup>3</sup> With respect to the reference red noise spectrum with the same variance.

positive AMV pattern can lead to a negative NAO phase (NAO $-$ ).

However, there are several disagreements on some aspects of this proposed mechanism. One of them concerns whether the buoyancy fluxes that lead to positive density anomalies are created by local surface buoyancy fluxes that are linked to NAO+ or are associated with advective transports [see Buckley and Marshall (2016) for further discussion]. Another disagreement concerns whether the positive density anomalies are salinity or temperature dominated. A third question is the realism of the links between the LS DWF and changes in AMOC for two reasons: 1) the observations suggest that there is very little export out of the LS, although available time series are relatively short (Pickart and Spall 2007; Lozier et al. 2019); and 2) many models tend to have an overproduction of LS water compared to observations (Li et al. 2019). We also note that several recent studies have suggested that the SST anomaly pattern associated with AMV, or its basin-averaged time series, can be reproduced (or driven) either by external radiative forcing (e.g., Booth et al. 2012; Bellucci et al. 2017; Murphy et al. 2017) or stochastic atmospheric forcing (e.g., Clement et al. 2015; Cane et al. 2017) without a role for the ocean. As discussed in detail in Zhang et al. (2019) (and references therein), many subsequent studies have shown that neither of these two mechanisms can explain many other observed fundamental elements and fingerprints of AMV whose development requires an important role for ocean dynamics.

In this study, we investigate robust and nonrobust aspects of AMOC variability characteristics within the context of the prevailing low-frequency variability mechanism introduced above in a *single coupled modeling framework*, namely the Community Earth System Model, version 1, (CESM1; formerly known as CCSM). By using a single framework, we aim to identify sensitivities with simulations that reference the same control experiment with each simulation differing from it primarily only in one particular aspect—an approach that is not possible when simulations are compared from different coupled models or even from different versions of the same model. Thus, our method is clean in the sense that it avoids rather complicated comparisons and ambiguous interpretations and attributions of differences in AMOC variability among simulations that involve numerous numerical, physical, and forcing differences. Specifically, we perform several sets of 600-yr-long preindustrial control simulations which include experiments where a few loosely constrained ocean model parameters are changed within acceptable ranges, as well as experiments where atmospheric initial conditions are perturbed at round-off level. While the

parameter sensitivity experiments follow from and expand upon our previous work that suggests that details of some parameterizations can impact AMOC variability as discussed above, initial condition perturbation simulations provide a reference context to evaluate changes. We pay particular attention to the stationarity of AMOC properties to determine if such 600-yr simulations are adequate to robustly determine AMOC characteristics. This is important because a majority of the coupled control simulations analyzed in AMOC-related studies have been integrated for about 500 years, consistent with the minimum integration length recommendation by CMIP (e.g., CMIP6; Eyring et al. 2016). Given initial transients, integration lengths analyzed in published studies are likely even shorter. Thus, our study represents a dedicated effort to quantify and consolidate the impacts of a limited set of diverse sources of uncertainty in AMOC variability, while providing an assessment of robust and nonrobust aspects of such variability in CESM. A description of the numerical experiments is given in section 2. In section 3, we present our results. Conclusions along with a discussion are in section 4.

## 2. Numerical experiments

The CESM1 is a fully coupled model of Earth's climate system. We use the same model version as in the CESM Large Ensemble (LE) preindustrial simulation (Kay et al. 2015) except that 1) we employ an older version of the ozone concentration dataset identical to that used in the CCSM4 simulations (Gent et al. 2011) and 2) we do not activate the ocean biogeochemistry module and the atmospheric carbon dioxide cycle in favor of performing more and longer sensitivity experiments that would not have been possible otherwise. The reason for this latter choice is that both of these features were diagnostic in CESM LE simulations with no impact on the simulated climate. The components of the CESM LE version are the Community Atmosphere Model, version 5 (CAM5; Neale et al. 2012), the Parallel Ocean Program version 2 (POP2; Smith et al. 2010; Danabasoglu et al. 2012a), the Community Land Model, version 4 (CLM4; Lawrence et al. 2012), and the Sea Ice Model, version 4 (CICE4; Holland et al. 2012). All components use nominal 1° horizontal resolution. We refer to Gent et al. (2011), Hurrell et al. (2013), and Kay et al. (2015) for details of the coupled model framework.

All the new simulations performed for this study are integrated for 600 years, starting from model date 1 January 402 of the 2200-yr LE preindustrial simulation, avoiding the initial adjustment period of the coupled system. The 600-yr integration length is affordable

TABLE 1. Brief descriptions of the sensitivity experiments.

Expt name	Description
CONT	Control
IC1	Round-off-level perturbations are applied to the initial air temperature field
IC2	Round-off-level perturbations are applied to the initial air temperature field
MBL	Isopycnal and thickness diffusivity values in the surface boundary layer are reduced from 3000 to 2000 $\text{m}^2 \text{s}^{-1}$
MDO	Minimum isopycnal and thickness diffusivity values in the deep/abyssal ocean are increased from 300 to 600 $\text{m}^2 \text{s}^{-1}$
SUBM	Minimum length scale of mixed layer fronts in the submesoscale mixing parameterization is reduced from 5 to 3.3 km
HV	Interior horizontal viscosity is reduced from 600 to 300 $\text{m}^2 \text{s}^{-1}$
VBD	Vertical background diffusivity is reduced from $0.17 \times 10^{-4}$ to $0.10 \times 10^{-4} \text{m}^2 \text{s}^{-1}$
LE1	Large Ensemble preindustrial simulation for years 401–1000
LE2	Large Ensemble preindustrial simulation for years 1001–1600
LE3	Large Ensemble preindustrial simulation for years 1601–2200

and certainly comparable to what is found in the literature. A list of the experiments is provided in Table 1. The control experiment (CONT) uses the coupled model described above with the default parameter settings in all its components. Our primary set of experiments consists of five sensitivity simulations initially intended to investigate impacts of a few loosely constrained ocean model parameter values on AMOC variability. In these experiments, select parameters are changed within acceptable ranges as described below. Because these changes represent relatively small perturbations to the coupled system, they do not change the mean state of the climate in a significant way and there are no strong or long transient adjustments (not shown).

In the ocean model, the effects of diabatic mesoscale fluxes within the surface diabatic layer are included using a near-surface eddy flux parameterization in which these fluxes become lateral—rather than along isopycnals—in the surface boundary layer (Ferrari et al. 2008; Danabasoglu et al. 2008). Furthermore, both the isopycnal and thickness diffusivity coefficients for the Gent and McWilliams (1990) isopycnal transport parameterization vary identically in the vertical, following a buoyancy frequency ( $N$ )-dependent prescription from Ferreira et al. (2005) and Danabasoglu and Marshall (2007) with enhanced diffusivity values in the upper ocean and much smaller values at depth. In this approach, the largest (referred to as the reference) diffusivities occur within the surface boundary layer. In experiment MBL (for mesoscale boundary layer), this reference isopycnal and thickness diffusivity value is reduced from 3000 to 2000  $\text{m}^2 \text{s}^{-1}$ . In a complementary experiment denoted as MDO (for mesoscale deep ocean), the minimum isopycnal and thickness diffusivity applied in the deep ocean is increased from 300 to 600  $\text{m}^2 \text{s}^{-1}$ . These diffusivity choices are within the ranges of both theoretically and observationally based estimates (e.g., Abernathy and Marshall 2013; Bates et al. 2014; Cole et al. 2015), and they are expected to

influence both advective and diffusive tracer transports, and hence impacting lateral tracer gradients.

The ocean model represents the restratification effects of submesoscale mixed layer eddies via the mixed layer eddy parameterization of Fox-Kemper et al. (2008) as implemented by Fox-Kemper et al. (2011). As discussed in the latter, a rescaling of this parameterization for use in non-eddy-resolving coarse-resolution ocean models introduces a length scale  $L_f$  to represent the typical local width of mixed layer fronts. The scale  $L_f$  is suggested to be similar in magnitude to the mixed layer deformation radius given by  $NH/f$ , where  $H$  is the mixed layer depth and  $f$  is the Coriolis parameter. Because the parameterized submesoscale velocities are inversely proportional to  $L_f$ , to prevent unbounded velocities and associated mixed layer transports, model implementations of the parameterization limit the minimum value of  $L_f$  (i.e.,  $L_{f,\min}$ , to  $0.2 \leq L_{f,\min} \leq 5$  km). This limit range is based on some observational and high-resolution modeling studies (see Fox-Kemper et al. 2011). By default,  $L_{f,\min} = 5$  km in CONT, chosen to prevent overly large mixed layer transports in comparison to the typical maximum overturning transports. In experiment SUBM (for submesoscale),  $L_{f,\min}$  is reduced to 3.33 km. Because changes in  $L_{f,\min}$  impact the high-latitude values of  $L_f$  most strongly, where  $f$  is large, this change is anticipated to influence parameterized contributions to the properties of the deep waters formed in the LS region.

The anisotropic horizontal viscosity formulation (e.g., Large et al. 2001; Danabasoglu et al. 2012a) uses 600  $\text{m}^2 \text{s}^{-1}$  as the minimum (interior) viscosity in the east–west direction. In the north–south direction, the minimum viscosity increases from an equatorial value of 600 to 1200  $\text{m}^2 \text{s}^{-1}$  by 45° latitude. Although it is desired to have physically based values, the magnitudes of these viscosities are usually specified to control numerical (grid-scale) noise, as is also the case in the present ocean model. In experiment HV (for horizontal viscosity), the

minimum horizontal viscosity values are lowered in both directions: it is set to  $300\text{ m}^2\text{ s}^{-1}$  for the east–west direction, and it increases from an equatorial value of 300 to  $600\text{ m}^2\text{ s}^{-1}$  by  $45^\circ$  latitude in the north–south direction. These reductions produce somewhat noisier solutions.

Our final parameter sensitivity experiment VBD (for vertical background diffusivity) involves reduction of the background vertical diffusivity from  $0.17 \times 10^{-4}$  to  $0.10 \times 10^{-4}\text{ m}^2\text{ s}^{-1}$ . This lower background value is certainly within observational estimates (e.g., Waterhouse et al. 2014; MacKinnon et al. 2017) and it is the same as used in CCSM3 for the nontidal background mixing (Danabasoglu et al. 2006).

These experiments are complemented by two additional sets of simulations to evaluate the changes in AMOC variability and mechanisms seen in the above-described parameter sensitivity experiments in the context of changes due to nonstationarity and/or initialization effects. The first set consists of two experiments labeled as IC1 and IC2 (for initial condition) in which round-off perturbations are applied to the initial air temperature field. Otherwise, IC1 and IC2 are identical to CONT.

The second set involves splitting the 2200-yr LE pre-industrial simulation into three 600-yr segments, starting at year 401. Thus, we treat years 401–1000, 1001–1600, and 1601–2200 as three separate experiments labeled as LE1, LE2, and LE3, respectively. With the majority of the adjustments/drifts in AMOC and in both global and basin-scale horizontal-mean potential temperature and salinity occurring during the first 400 years, such a split may be interpreted as three different integrations in which the entire coupled system is initialized differently. While any deviations in variability characteristics among LE1, LE2, and LE3 highlight nonstationarity associated with AMOC variability, LE1 differences from CONT can be attributed to use of a different ozone concentration dataset.

Because we are primarily interested in large-scale, subthermocline characteristics of AMOC variability and because the impacts of parameterized mesoscale and submesoscale eddies are confined to the upper few hundred meters in the North Atlantic, for simplicity we use Eulerian-mean (i.e., resolved) AMOC in our analysis. Furthermore, we choose the maximum AMOC transport at  $45^\circ\text{N}$  time series as our primary index. In our experience, such a *high-latitude* AMOC index represents mid- to high-latitude AMOC variability that is more strongly associated with buoyancy forcings and related changes in the northern North Atlantic than those of lower latitudes. We note, however, that we can expect significant differences in spectral characteristics

of various AMOC indices that include maximum transports at a given latitude or the first principal component (PC1) time series as shown by Yeager and Danabasoglu (2012). In addition, we use AMOC in latitude–depth space because our present analysis is focused on deciphering robust and nonrobust elements of AMOC variability in the context of previous literature primarily focused on AMOC in depth space.

Our analysis mainly uses annual-mean fields. The exceptions are the boundary layer depth (BLD) where March-mean data are used, and the regression analysis for heat and salt budgets as well as for the surface buoyancy fluxes where monthly-mean fields are employed. We use standard correlation, regression, spectral and wavelet analysis, and empirical orthogonal function (EOF) methods. During the first phase of our study, we used annual-mean (i.e., raw) data to establish benchmark relationships among many fields of interest. We then repeated the same analyses using various low-pass-filtered time series. Only after establishing that both the raw and low-pass-filtered analyses produce similar results have we opted to present our findings using a 10-yr low-pass Lanczos filter (Duchon 1979) to emphasize decadal and longer time scales. The exceptions are the spectral and wavelet analyses, which use only annual-mean data. However, a three-point modified Daniell filter in frequency domain is applied in spectral plots. We note that time series are detrended using a linear fit prior to analysis. The calculation of confidence levels takes into account any reductions in the effective degrees of freedom that result from temporal smoothing via lag-1 serial autocorrelations.

### 3. Results

We start with an evaluation of the AMOC mean-state differences between the experiments, considering 600-yr averages. The time-mean AMOC from CONT (Fig. 1, top-left panel) shows a clockwise circulation cell (positive in the figure) associated with the NADW as its primary feature with a maximum transport of about 26 Sv, occurring near  $35^\circ\text{N}$  and 1-km depth. While the NADW penetration depth reaches the ocean bottom north of about  $20^\circ\text{N}$ , the transport associated with the Antarctic Bottom Water (AABW) remains weak. The spatial structure of AMOC and its features are very similar to those of CCSM4 AMOC (Danabasoglu et al. 2012b).

The remaining panels of Fig. 1 illustrate the time-mean differences of AMOC in the sensitivity experiments from that of CONT. The two experiments MBL and MDO, in which the mesoscale eddy diffusivity coefficients are changed, show the largest differences from

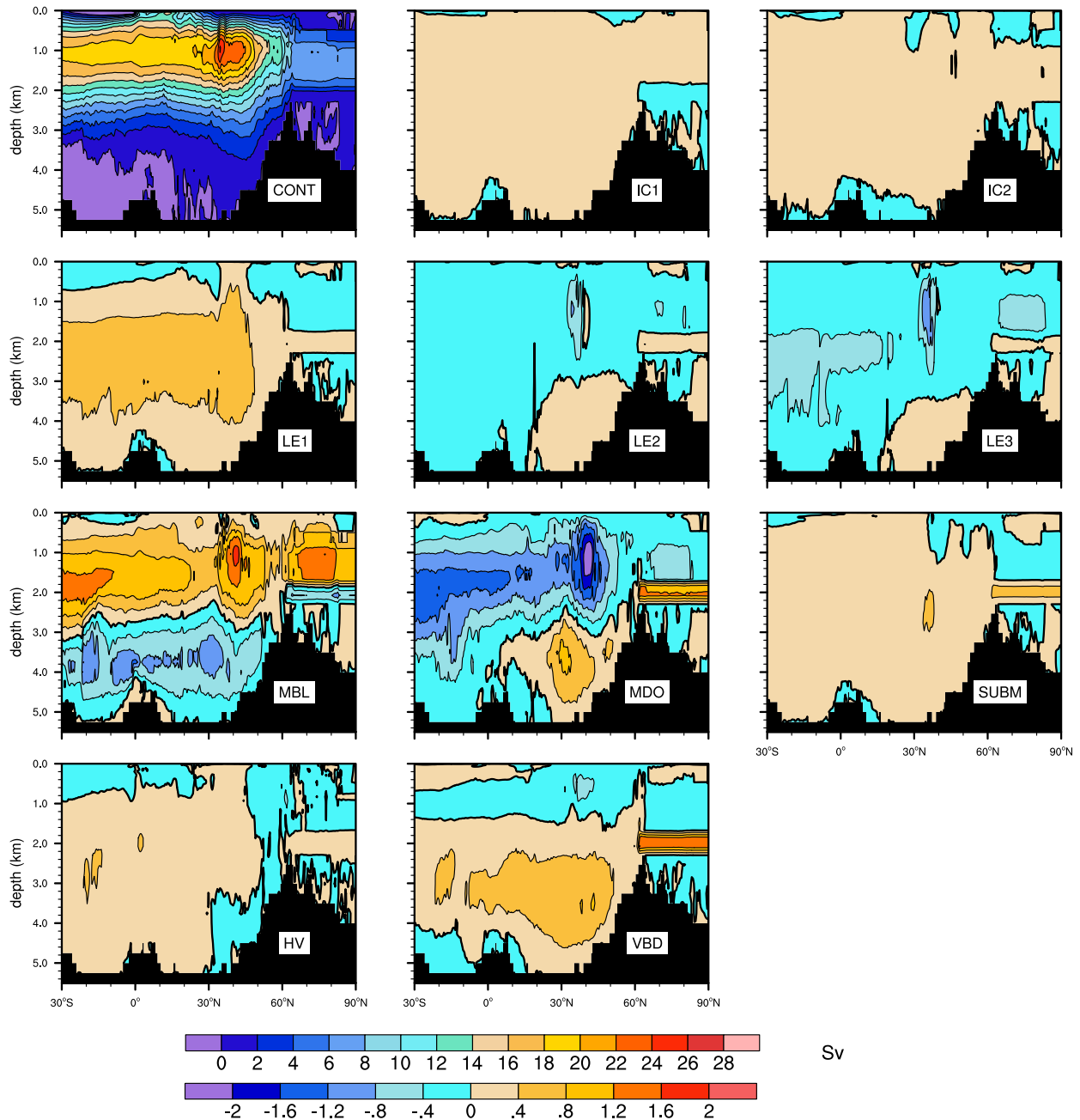


FIG. 1. (top left) Time-mean AMOC from CONT (top color bar) and (other panels) differences of time-mean AMOC in the sensitivity experiments from CONT (bottom color bar). The positive and negative contours indicate clockwise and counterclockwise circulations, respectively.

CONT. In MBL, the difference distributions are primarily positive at depths shallower than roughly 3 km and negative at deeper levels south of about 60°N. These changes indicate overall strengthening—by as much as 1.6 Sv—and shallowing of the NADW cell. In accordance, the AABW cell becomes slightly stronger and occupies a larger fraction of the abyssal North Atlantic.

Changes in MDO are largely opposite to those of MBL. Specifically, the NADW cell gets noticeably weaker throughout the Atlantic basin by a maximum of about 1.6 Sv, while it penetrates deeper with a slightly larger transport roughly below 3-km depth and north of 20°N. Furthermore, the AABW remains weak in MDO as in CONT. The stronger and weaker NADW transports

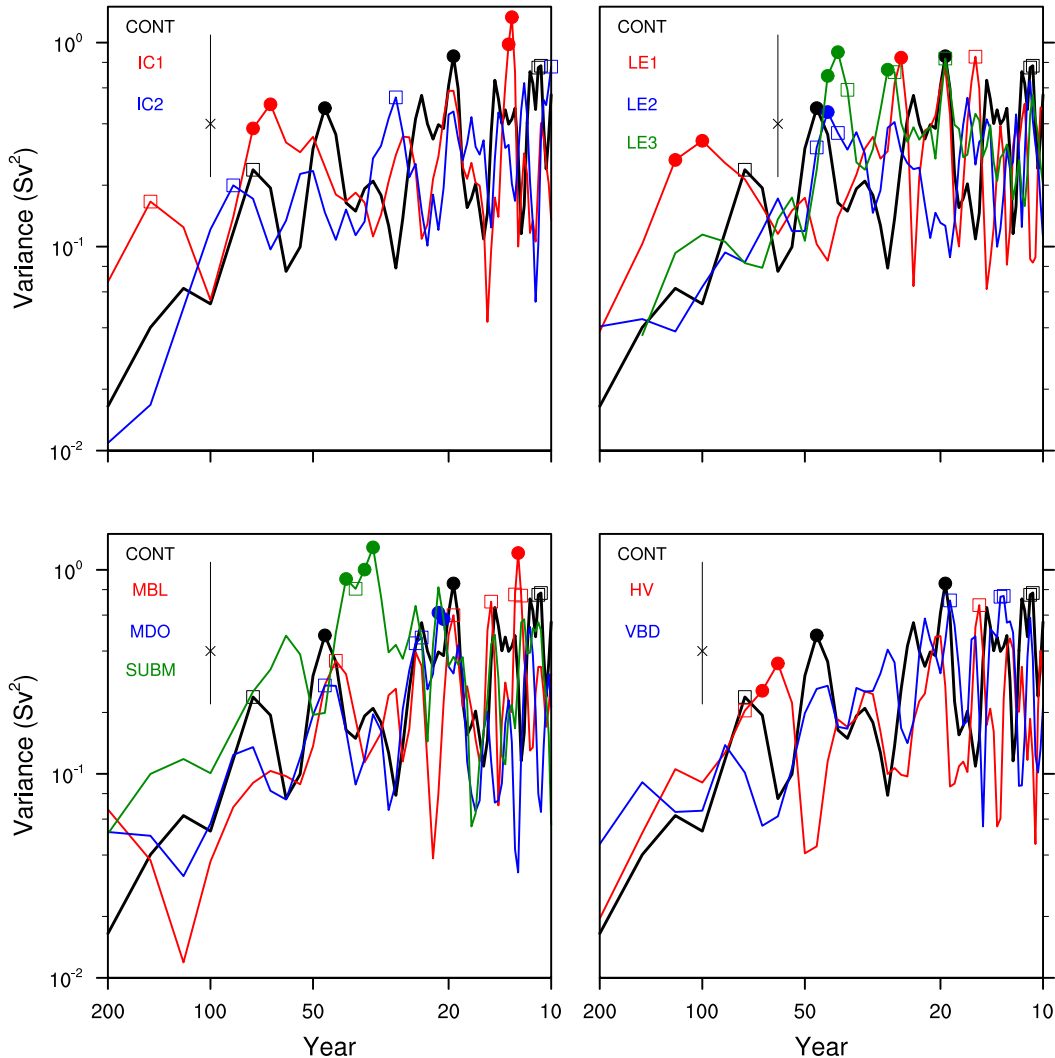


FIG. 2. Power spectra of the annual-mean AMOC index time series for all the cases. The open squares and filled circles denote the 90% and 95% confidence levels, respectively, for each case individually, based on the respective reference red noise spectrum with the same total variance as that case. The vertical lines indicate the 90% confidence interval and they are the same in all panels. The spectra are smoothed using a three-point modified Daniell filter in frequency domain. CONT is included in all panels.

with smaller and larger mesoscale diffusivity coefficients in MBL and MDO, respectively, are consistent with the findings of Danabasoglu and McWilliams (1995), where such changes were attributed primarily to reduced (increased) density gradients with larger (smaller) diffusivity values.

The time-mean AMOC distributions and transport strengths for the other cases are more similar to those of CONT. There are no appreciable changes in IC1, IC2, and HV. In LE2 and LE3, the NADW cell shows broad but very small weakening with a maximum reduction of about 0.8 Sv near the maximum AMOC transport location. In LE1 and SUBM, there is a general enhancement

of the NADW transport by  $<0.8$  and  $<0.4$  Sv, respectively. Last, there are minor changes of opposite signs in the upper ocean ( $-0.4$  Sv) and deep ocean (0.8 Sv) in VBD. We note that the changes centered at 2-km depth north of  $60^{\circ}$ N evident in some panels are associated with changes in the insertion depth and amount of the overflow product waters [see Danabasoglu et al. (2010) for details of the overflow parameterization used in the CESM simulations].

The power spectra of the AMOC index time series are shown in Fig. 2. The spectra are smoothed using a three-point modified Daniell filter in frequency domain. The figure includes two different measures of statistical

confidence intervals. The first measure follows common practice and determines statistical significance of spectral peaks in each spectrum individually with respect to a reference red noise spectrum with the same total variance as that case. The second measure provides a confidence interval based on the chi-squared distribution, taking into account the filter width and weights, to determine if the spectra from all the cases are statistically distinguishable from each other. Because the figure uses a log scale for variance, the extent of this confidence interval is independent of frequency and is shown as the same single vertical line in each panel. Thus, when comparing any two spectra, this confidence interval should be applied at each frequency to its spectral value. With respect to individual reference red noise spectra, the figure shows that the time scales of AMOC variability differ among the cases, with the dominant time scales ranging from decadal to multidecadal to even centennial. Considering the peaks with  $\geq 95\%$  confidence levels, the dominant time scales—with approximate peak periods/ranges given in years in parentheses—are decadal in IC1 (15) and MBL (15); multidecadal in CONT (20 and 45), LE1 (30), LE2 (45), LE3 (25 and 40–45), MDO (20–25), and SUBM (30–40); and centennial in IC1 (65–80), LE1 (100–120), and HV (60–70). We note that CONT, IC1, LE1, and LE3 show significant peaks at multiple time scales. There are some distinct spectral peaks and ranges in IC2 and VBD as well, but the confidence level is  $\leq 90\%$ . Arguably, the most prominent feature of Fig. 2 is the large, multidecadal time scale peak in SUBM. However, when the 90% spectral confidence range is considered, it is difficult to assess whether the *significant* peaks identified above in a particular case lie outside the range of variability of another case. For example, the dominant multidecadal peak of SUBM is statistically distinguishable from CONT and MDO, but not significantly different from LE1, LE2, and LE3. While a major conclusion here is that the time scales of AMOC variability are a nonrobust characteristic of AMOC in CESM simulations of 600-yr length, there is also substantial sampling uncertainty that limits our ability to robustly detect differences in AMOC variability among the cases.

We next consider statistical stationarity of AMOC variability, performing a wavelet analysis for the AMOC index time series. The resulting spectra for all the cases are presented in Fig. 3, showing statistically significant periods that are broadly consistent with those of Fig. 2. However, a striking feature of the wavelet distributions is that these periods are not stationary in time, varying considerably during the course of the simulations. For example, in SUBM the significant variability periods are

about 20–40 years during years 480–620, about 50–80 years during years 600–720, and about 25–40 years during years 780–860. Noting that LE1, LE2, and LE3 actually represent one continuous simulation, robust characterization of AMOC variability properties requires multimillennium-scale simulations at the very least. Unfortunately, due to resource limitations, such long simulations are not performed by many modeling groups, and they are not required by CMIP6 (Eyring et al. 2016).

To obtain patterns of the dominant spatial variability modes, we regress AMOC from each case onto its respective AMOC index time series. Figure 4 shows the resulting spatial patterns for CONT and SUBM only, because the other cases have very similar distributions. We include SUBM in this comparison to show that its strong multidecadal variability is still associated with a very similar spatial pattern as in the other cases. The regression distributions have a single cell pattern that covers the entire Atlantic basin south of  $60^\circ\text{N}$ , corresponding to overall strengthening and deeper penetration of the NADW cell in its positive phase. The maximum regression values are about 0.9 and 1.2 Sv per unit index in CONT and SUBM, respectively.

The CESM ocean component uses an overflow parameterization to represent the Denmark Strait and Faroe Bank Channel density-driven overflows in the northern North Atlantic (Briegleb et al. 2010; Danabasoglu et al. 2010). The parameterization accounts for exchanges of such dense waters—formed in the Nordic seas—through narrow channels and straits, associated entrainment, and subsequent injection of the resulting overflow product waters into the deep basins. In Yeager and Danabasoglu (2012) and Danabasoglu et al. (2012b), we investigated the relationship between the AMOC and overflow transports considering only two simulations. Here, we take advantage of our suite of simulations and revisit this relationship to determine its robustness. Figure 5 shows the AMOC index time series correlated with the combined Denmark Strait and Faroe Bank Channel overflows parameterized product water transport (PWT) time series, indicating that in all the experiments AMOC (or NADW) strengthening leads any increases in PWT by about 7 years in the ensemble mean. When PWT leads, the largest correlations are negative occurring at 2–3-yr leads, suggesting that the NADW transport weakens. The respective correlation coefficients are 0.52 and  $-0.34$  for the ensemble mean. These findings indeed confirm the robustness of the results of Yeager and Danabasoglu (2012) and Danabasoglu et al. (2012b), where reductions in AMOC in the upper ocean with larger PWT are found to be associated with enhanced

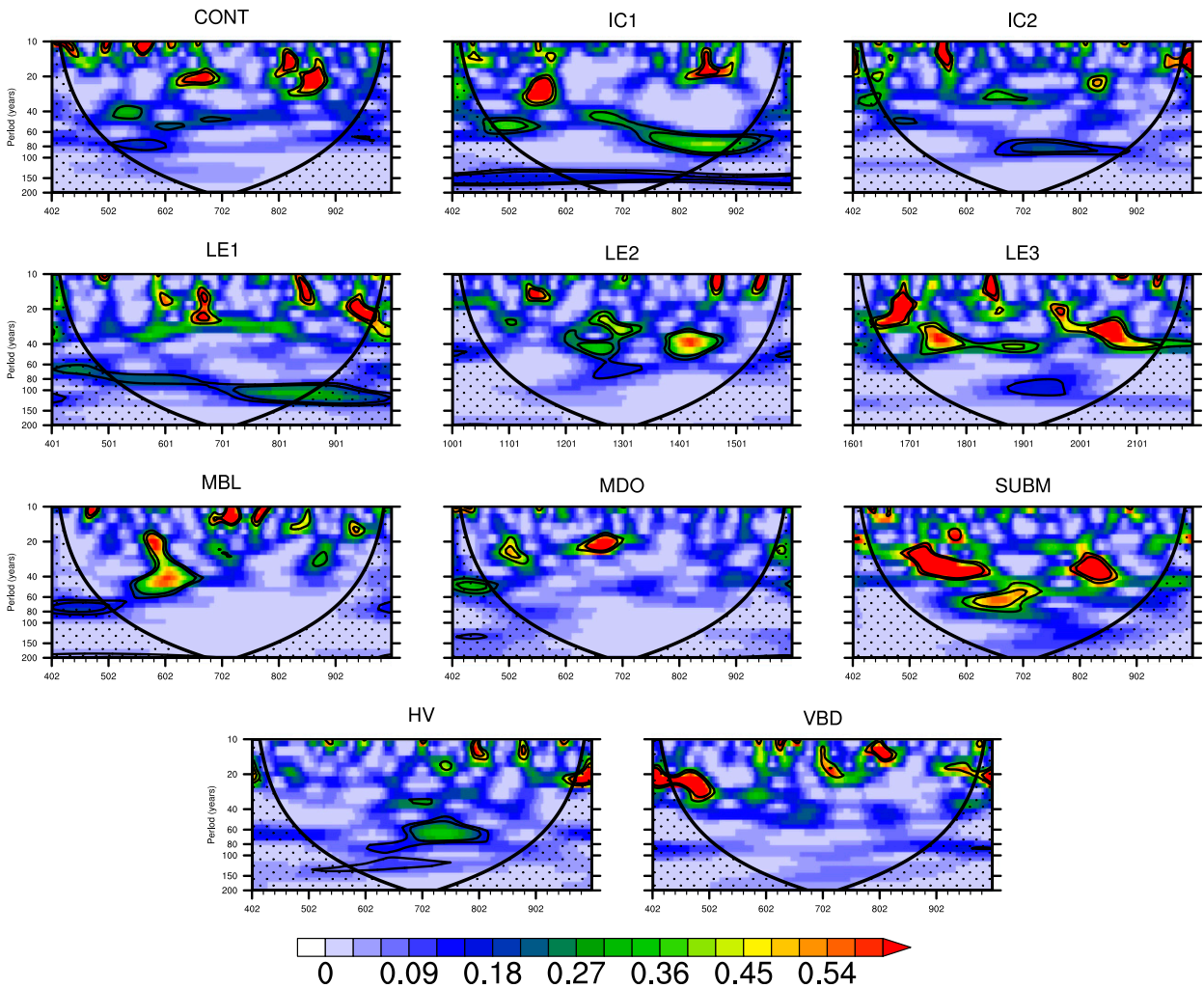


FIG. 3. Wavelet spectra of the annual-mean AMOC index time series for all the cases. The thick black lines with the dotted regions demarcate the cone of influence where the edge effects influence the spectra. The black contours indicate regions of 90% and 95% confidence levels. The unit is  $\text{Sv}^2$ .

LS stratification and subsequent reduction in LS convection, noting that the LS stratification is maintained by the overflow waters. The AMOC index versus PWT time series lead-lag relationships found here are in contrast to Hawkins and Sutton (2008), where the overflow transports lead enhanced AMOC by a few years. As discussed in Danabasoglu et al. (2012b) in detail, this major difference can likely be attributed to parameterized overflows in CCSM/CESM simulations versus their explicit representation via artificially deepened topography in the Denmark Strait overflow region in the model analyzed in Hawkins and Sutton (2008). This results in unrealistically high overflow transports (compared to available observations), with additional differences in major deep convection regions (Labrador Sea in CESM vs Nordic seas) also playing a role.

Figure 6 shows time series correlations between the AMOC index and the March-mean BLD, upper-ocean density  $\rho_{uo}$ , subpolar gyre transport (SPG), and NAO. The reason for considering these fields in this analysis is because they are implicated in the prevailing low-frequency variability mechanism discussed in the introduction, with the addition of a SPG index to monitor its associated changes. Here, BLD,  $\rho_{uo}$ , and SPG represent averages within the LS box region bounded by  $50^{\circ}$ – $65^{\circ}\text{N}$ ,  $60^{\circ}$ – $35^{\circ}\text{W}$  (identified in Fig. 8). We use this LS domain in our analysis as it has been identified in many previous studies as an important region influencing AMOC variability (e.g., Danabasoglu 2008; Danabasoglu et al. 2012b). The upper-ocean density is an average over the upper 203 m. Additionally, we use March-mean BLD as it attains its maximum in March. It is calculated by the  $K$ -profile parameterization

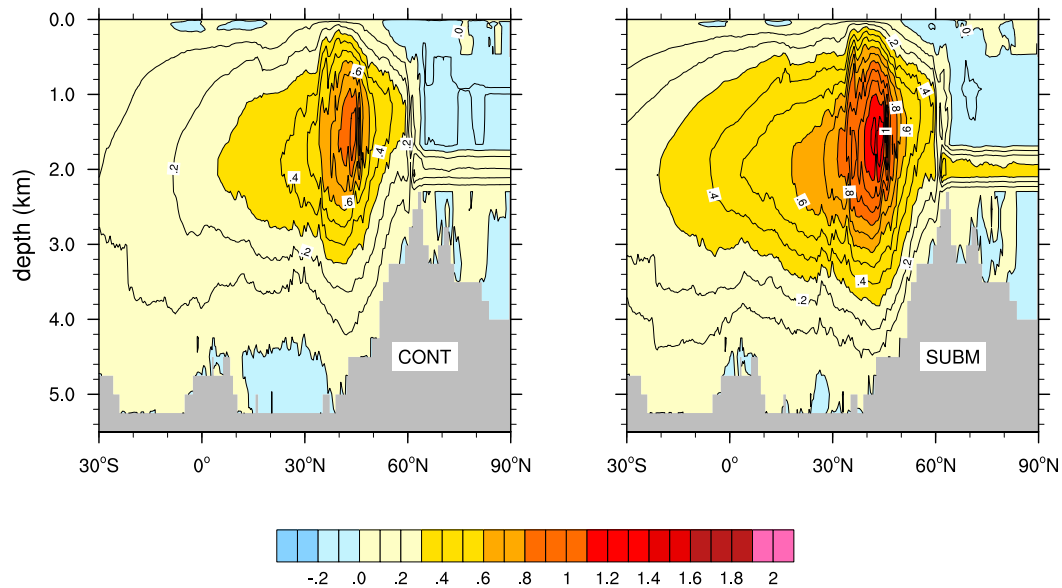


FIG. 4. AMOC regressions onto the respective AMOC index time series for (left) CONT and (right) SUBM. The contour intervals are 0.1 Sv per unit index. The positive and negative contours indicate clockwise and counter-clockwise circulations, respectively. The time series are 10-yr low-pass filtered.

vertical mixing scheme (KPP; Large et al. 1994) as the shallowest depth at which a bulk Richardson number exceeds a specified critical Richardson number for the first time. The NAO is defined as the wintertime (December–March) sea level pressure PC1 time series and the corresponding EOF shows a stronger-than-normal subtropical high pressure center in its positive phase. In the figure, the solid lines represent the ensemble-mean correlations from all the experiments and the color shadings indicate the envelope of individual experiment correlations. A very robust finding is that in all the simulations, the BLD,  $\rho_{uo}$ , and NAO time

series lead the AMOC index by 2–3 years. The largest (negative) correlations between the AMOC and SPG indices occur at lag 0, indicating simultaneous strengthening of AMOC and SPG transports. These results are consistent with those from CCSM4 discussed in Danabasoglu et al. (2012b). We note that the NAO–AMOC relationship depicted in Fig. 6 appears to be more robust with less ensemble spread than in the CMIP5 historical simulations analyzed in Xu et al. (2019). In addition to longer integration lengths of our preindustrial control simulations compared to the historical experiments, our choice of a *high-latitude*

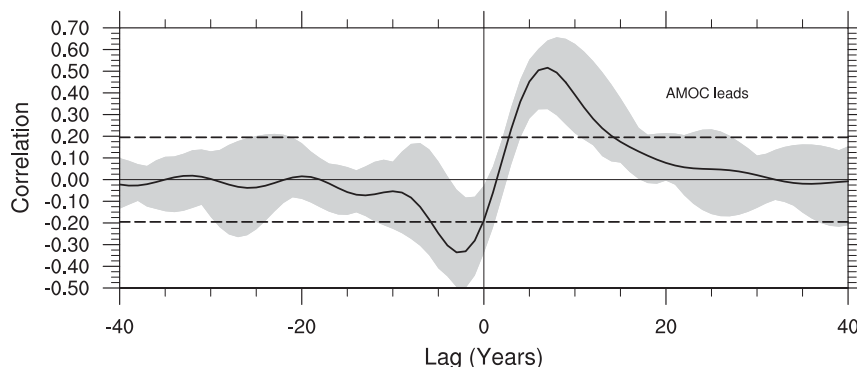


FIG. 5. AMOC index time series correlations with the combined Denmark Strait and Faroe Bank Channel overflows product water transport time series. The thick black line represents the ensemble-mean correlation of all the experiments, and the shading indicates the envelope of individual experiment correlations. AMOC index leads for positive lags. The dashed lines show the 95% confidence level. The time series are 10-yr low-pass filtered.

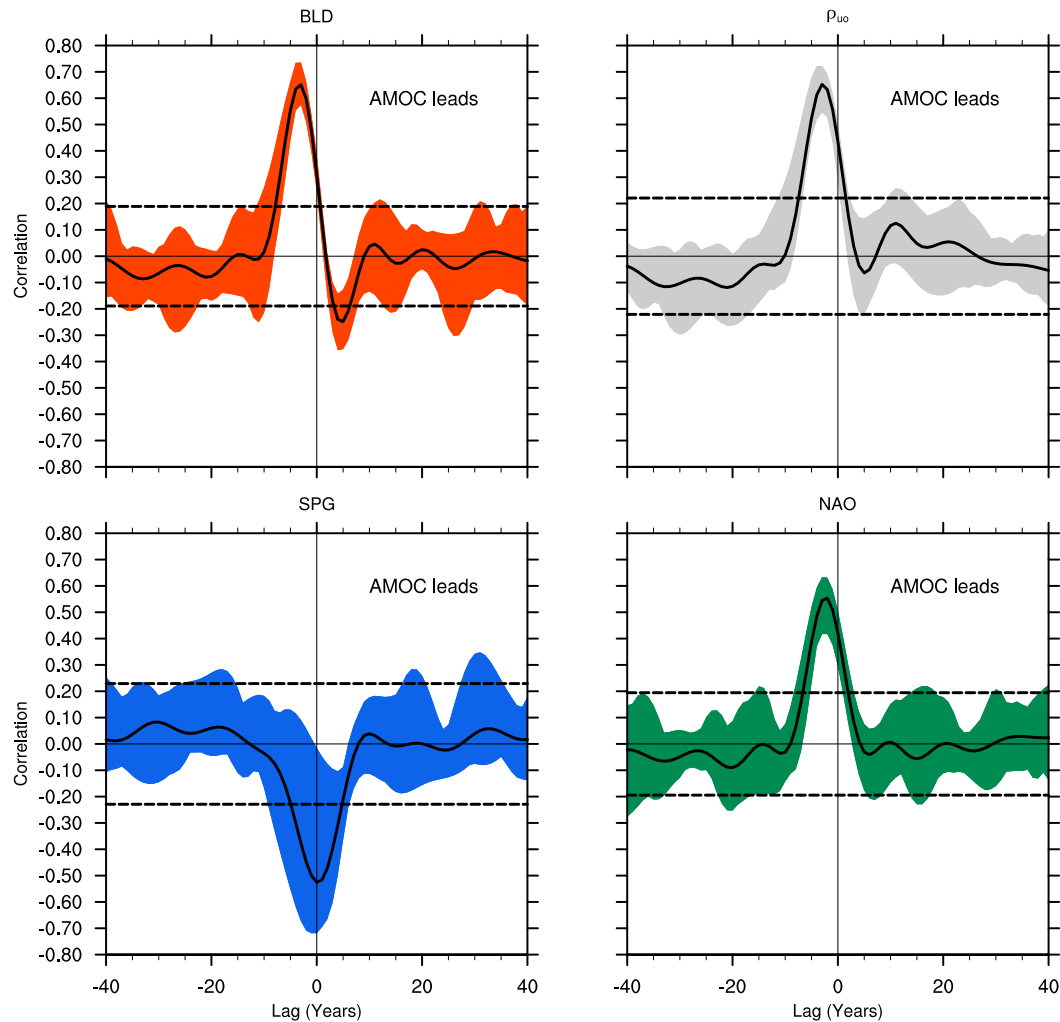


FIG. 6. AMOC index time series correlations with those of the (top left) March-mean boundary layer depth (BLD), (top right) upper-ocean density ( $\rho_{uo}$ ), (bottom left) subpolar gyre transport (SPG), and (bottom right) North Atlantic Oscillation index (NAO). BLD,  $\rho_{uo}$ , and SPG represent averages within the Labrador Sea region identified in Fig. 8. The thick black lines represent the ensemble-mean correlations of all the experiments, and the color shadings indicate the envelope of individual experiment correlations. AMOC index leads for positive lags. The dashed lines show the 95% confidence level. The time series are 10-yr low-pass filtered.

AMOC index<sup>4</sup> that is strongly associated with the buoyancy forcings in the northern North Atlantic certainly strengthens this robustness. Additionally, external forcings during the historical period can obscure these relationships, as discussed in Klavans et al. (2019) for the NAO–AMV relationship.

To determine whether the density anomalies are temperature or salinity dominated, especially prior to an AMOC intensification, Fig. 7 shows the regression coefficients between the AMOC index and the  $\rho_{uo}$  time series along with the temperature  $\rho_T$  and salinity  $\rho_S$

contributions to the density anomalies for the LS box from all the simulations individually. As already indicated in Fig. 6 (top right), all the simulations show a significant positive density anomaly leading the AMOC index by 2–3 years. In a majority of the simulations (i.e., CONT, IC1, IC2, LE2, LE3, MBL, HV, and VBD) temperature contributes more strongly to the positive density anomalies than the salinity. Quantitatively, among these cases, the  $\rho_T$  contribution ranges from about 72% in MBL to a maximum of near 100% in IC1 with respect to the maximum positive density anomalies for each case. The  $\rho_S$  contributions to the peak density anomaly remain below 32% in these eight cases. However, this behavior is not robust across all the cases.

<sup>4</sup> As opposed to using a lower-latitude or PC-based index.

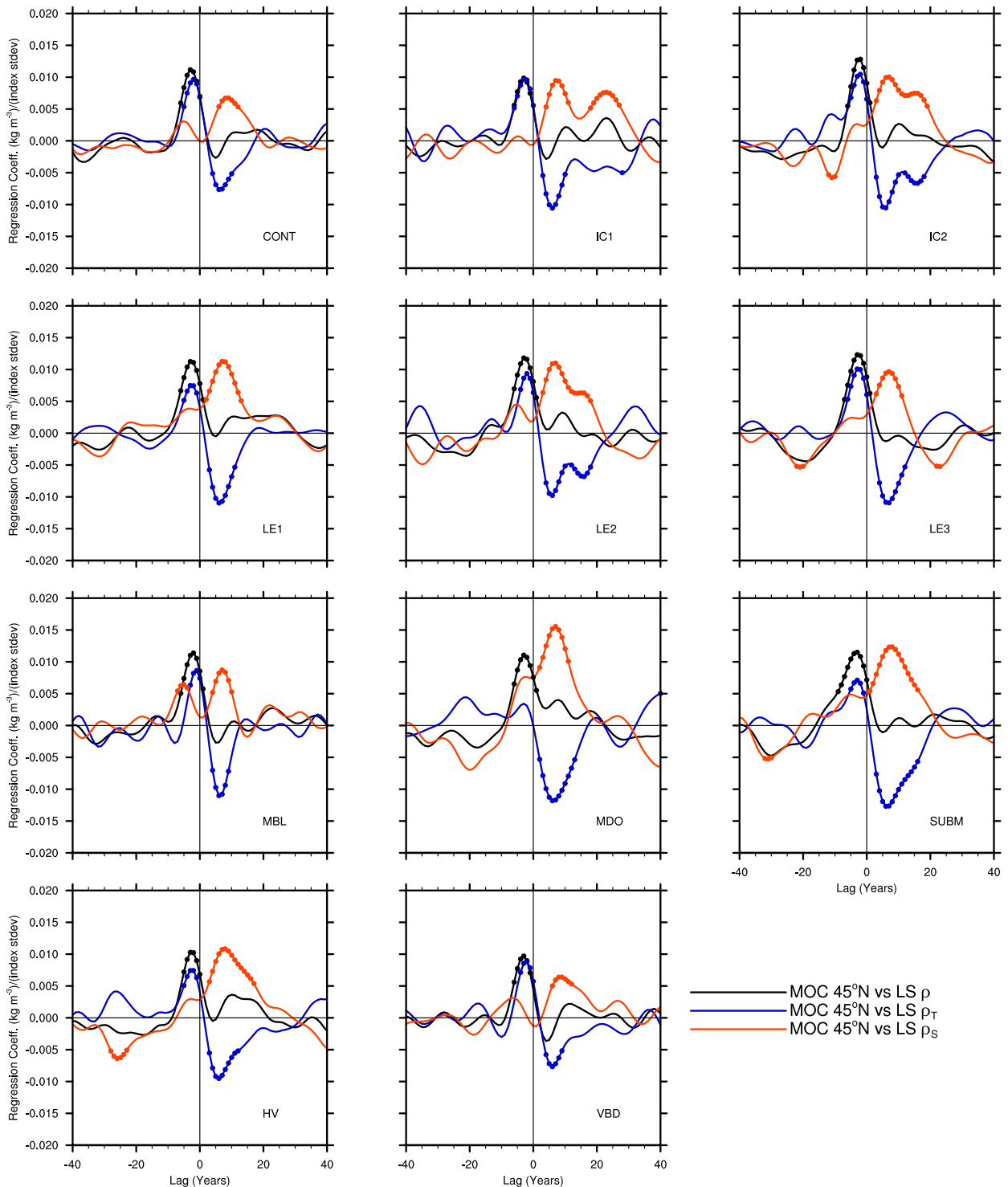


FIG. 7. The  $\rho_{uo}$  time series regressions onto the AMOC index time series within the LS box. The black line is for the total density. The temperature  $\rho_T$  and salinity  $\rho_S$  contributions to the total density are given by the blue and red lines, respectively. The regression coefficients are volume averaged, and they are in  $\text{kg m}^{-3}$  per unit index. The dots indicate when the corresponding correlations (not shown) have >95% confidence level. AMOC index leads for positive lags. The time series are 10-yr low-pass filtered.

Specifically, salinity contributes more strongly in MDO with  $\rho_S$  accounting for 67% of the peak positive density anomaly. In the remaining two cases, LE1 and SUBM, temperature and salinity contributions are more comparable to each other with 65% and 35% in LE1 and 62% and 38% in SUBM for  $\rho_T$  and  $\rho_S$ , respectively. In contrast, what is robust across all the experiments is that, following an AMOC increase, the negative  $\rho_T$  and positive  $\rho_S$  anomalies compensate each other to a large degree, resulting in near-neutral density anomalies. This results from advection of warm and salty waters into the LS region associated with increased AMOC and SPG transports. We note that these compensating  $\rho_T$  and  $\rho_S$  anomalies emerge rather quickly near lag 0 and persist at statistically significant levels for a broad range of lags, even extending beyond lag +25.

Spatial distributions of the regressions of the March-mean BLD and  $\rho_{uo}$  time series onto the AMOC index time series when the latter lags by 3 years are shown in Fig. 8. Here, these distributions are for CONT only, because the other cases have qualitatively very similar distributions. Also, the 3-yr lead for BLD and density roughly corresponds to the time of maximum correlation (and regression) between these fields and the AMOC index. The regression structures depicted in the figure are a robust aspect of AMOC-related variability in CESM simulations; similar distributions are also seen in the CCSM4 preindustrial control simulation (Danabasoglu et al. 2012b). The maximum BLD regression exceeds 150 m per unit index and its location (at about 55°N, 45°W) is not collocated with the climatological March-mean maximum BLD site (not shown). Rather, the largest BLD variability arises where the biggest mean BLD gradients are located in the southeastern LS. The region of positive density anomalies is rather broad, covering roughly the entire North Atlantic north of 45°N. The maximum density regression is  $>0.03 \text{ kg m}^{-3}$  per unit index and is located to the east of the maximum BLD regression region. The Nordic seas positive density anomalies largely reflect positive salinity anomalies. In contrast, the expansive negative density anomaly region east of North America between 25° and 45°N is due to a warm anomaly. Increasing AMOC transport may certainly contribute to this warm anomaly, but it is also forced by the atmosphere as evidenced by the positive surface heat flux anomalies during this time (not shown).

To understand the origins of the  $\rho_{uo}$  anomalies both prior to and following an AMOC intensification, we perform heat and salt budget analyses for the LS box region (down to 203-m depth), following the procedure described in Danabasoglu et al. (2012b). We first compute all the individual budget terms using monthly-mean

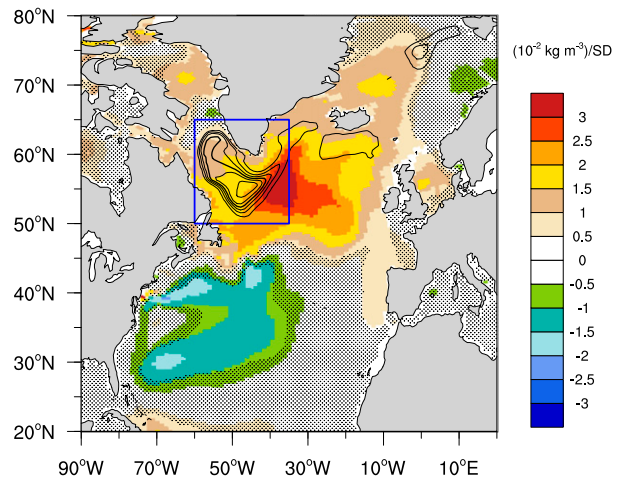


FIG. 8. Upper-ocean (0–203-m average) density (color) and March-mean boundary layer depth (contours) time series regressions onto the AMOC index time series when the latter lags by 3 years. The contour interval is 25 m per unit AMOC index for the boundary layer regression. No stippling indicates regions of  $>95\%$  confidence level. The boxed region shows the analysis domain for the Labrador Sea deep water formation site. The time series are 10-yr low-pass filtered.

data. We next create annual-mean, detrended time series for each component. Finally, these time series are 10-yr low-pass filtered and regressed onto the AMOC index time series. The total (or tendency) changes in heat and salt content are evaluated based on the differences of two subsequent January-mean values. The advection terms contain contributions from the resolved flow, parameterized mesoscale advection, and parameterized submesoscale advection. The surface fluxes contain all the contributions, including those from frazil sea ice formation. The diffusion terms are obtained as residuals, and represent the sum of the total parameterized horizontal, isopycnal, and vertical diffusive fluxes, including convection.

A summary of this heat and salt budget regression analysis is presented in Fig. 9 for all the experiments. In the figure, each symbol represents a budget term integral over lags  $-8$  to  $-2$  for before and over lags 0 to  $+6$  for after an AMOC intensification. These intervals are intended to roughly cover the time periods with changes that lead to the maximum  $\rho_{uo}$  anomalies. All the terms are converted to density anomalies using these time intervals<sup>5</sup> along with the thermal expansion and saline contraction coefficients for a representative

<sup>5</sup> The heat and salt (freshwater) budget analyses are performed in units of  $\text{W m}^{-2}$  and  $\text{kg m}^{-2} \text{ s}^{-1}$ , respectively. Conversion of the budget terms to equivalent density anomalies over a time interval requires an *integration* over given time lags.

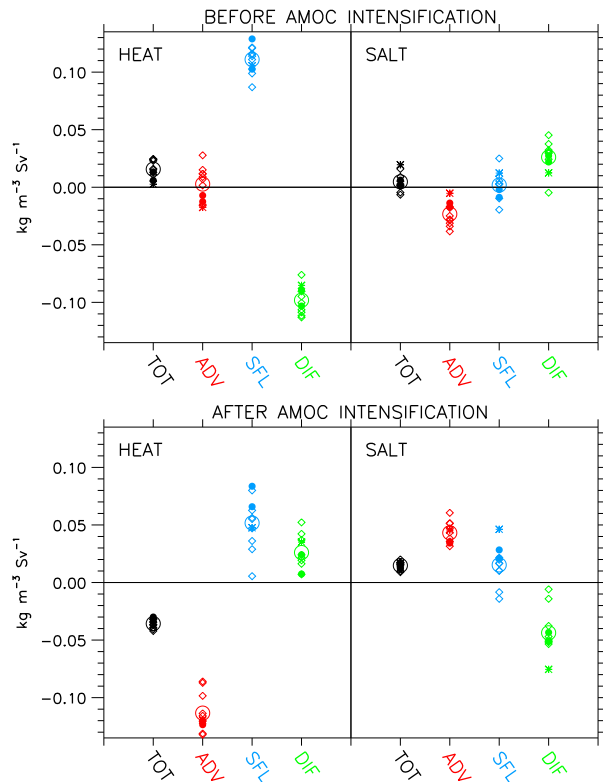


FIG. 9. Summary plot of the regressions of the heat and salt budget term time series onto the AMOC index time series for all the experiments for the LS region. The regressions are given for (top) before and (bottom) after an AMOC intensification. Each symbol represents a budget term integral for lags  $-8$  to  $-2$  in the top panel and lags  $0$  to  $+6$  in the bottom panel. With respect to their contributions to  $\rho_{uo}$  anomalies prior to an AMOC intensification, open diamonds are for the cases where  $\rho_T$  dominates, filled circles represent cases where  $\rho_T$  and  $\rho_S$  contributions are comparable, and stars are for the case in which  $\rho_S$  dominates. The large open circles denote the ensemble means. The budget terms are total (TOT), total advection (ADV), diffusion (DIF), and surface fluxes (SFL). All the terms are converted to density anomalies (see text). The time series are 10-yr low-pass filtered.

temperature and salinity pair of  $6^\circ\text{C}$  and 34.5 psu at the ocean surface. Furthermore, following the discussion related to Fig. 7, the cases are classified according to their contributions to  $\rho_{uo}$  anomalies prior to an AMOC intensification with open diamonds denoting the cases where  $\rho_T$  dominates; filled circles representing the cases where  $\rho_T$  and  $\rho_S$  contributions are comparable; and stars representing the case in which  $\rho_S$  dominates. The large open circles denote the ensemble-mean regressions. Before AMOC strengthens, temperature acts to increase density in all cases, and this is a balance between a large surface heat loss and a partial compensation by diffusive processes. The net advective contributions are much smaller than those of surface fluxes and diffusion with a near-zero ensemble mean. The salt contribution

to density varies across the cases, taking both positive and negative values. The primary balance is between positive contributions from the diffusion terms and negative contributions from advection. The surface flux contributions can be of either sign with an ensemble mean of near zero. The salinity domination of  $\rho_{uo}$  anomalies in MDO is clearly evident in the figure (stars), with MDO showing the largest (smallest) total salinity (temperature) contribution to density among all the cases. MDO is distinct with its anomalously weak salt advection term.

After AMOC intensification, the LS region warms and gets more saline in all the experiments, primarily due to increased advection of warm and salty waters into the subpolar North Atlantic with larger AMOC. As a result, density anomalies are much smaller (near-zero; see Fig. 7) in contrast to those preceding AMOC intensification. The negative advective contributions in heat are partly balanced by surface fluxes and, to a lesser extent, by diffusion. In addition to advection, surface fluxes—enhanced evaporative cooling—also act to increase density due to salt in a majority of the cases with diffusion significantly compensating both.

To investigate how the large surface heat loss is generated prior to an AMOC intensification, we apply the same regression procedure described above to the components of the surface heat and freshwater fluxes over the LS region. A summary of this analysis is presented in Fig. 10, showing individual surface flux component integrals over lags  $-8$  to  $-2$ . As before, all the terms are converted to density anomalies. The two largest contributions to the positive density anomalies come from sensible and latent heat fluxes. There is also a nonnegligible contribution from the longwave down component, although this flux is largely compensated by the longwave up component, resulting in near-zero net longwave contribution. The remaining fluxes are negligible. The sign of the total freshwater flux is not robust across the cases, with contribution of both signs and an ensemble mean of near zero. The dominant fluxes are evaporation and melt.

Finally, the regressions of the surface heat and freshwater flux components over the LS region onto the wintertime NAO (PC1) time series are presented in Fig. 11. Again, all the terms are converted to density anomalies using integrals over lags  $-5$  to  $0$  with respect to the NAO time series. This lag interval corresponds to lags  $-7$  to  $-2$  with respect to the AMOC index time series, accounting for NAO+ leading an AMOC intensification by about 2–3 years. The heat flux regressions in Fig. 11 show very similar dominant contributions of the latent and, particularly, the sensible heat fluxes to the total density anomaly as in Fig. 10.

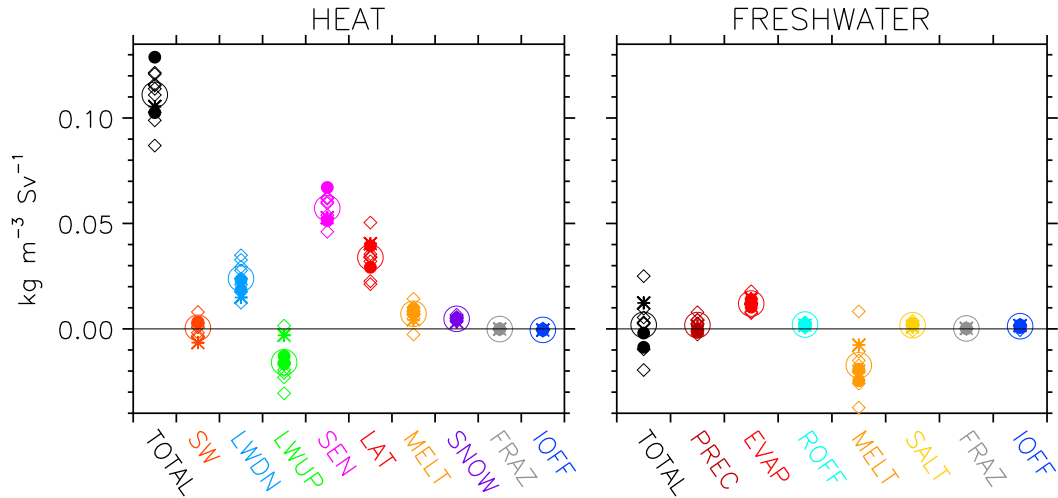


FIG. 10. Summary plot of the regressions of the (left) heat and (right) freshwater surface flux component time series onto the AMOC index time series for all the experiments for the LS region. The regressions are for before an AMOC intensification for lags  $-8$  to  $-2$ . The symbol convention is as in Fig. 9. The surface flux components are total (TOTAL); shortwave (SW), longwave down (LWDN), longwave up (LWUP), sensible (SEN), latent (LAT), melt heat and freshwater flux (MELT), heat flux due to snow (SNOW), heat and freshwater flux due to solid runoff (IOFF) melt, frazil ice formation (FRAZ), precipitation (PREC), evaporation (EVAP), liquid runoff (ROFF), and salt flux due to ice formation and melt (SALT). All the terms are converted to density anomalies. The time series are 10-yr low-pass filtered.

However, there is also a notable contribution from the melt term, indicating heat loss by the ocean due to ice melt. Prominent contributions from the sensible and latent components confirm that the NAO-related surface heat fluxes play a significant role in AMOC variability in all the experiments. The sign of the total freshwater flux is negative, primarily reflecting the melt term. Evaporation has a positive, but small contribution. It is interesting to note that MDO has the lowest total

heat flux regression with small sensible and latent—indeed, negative—component contributions.

#### 4. Conclusions and discussion

We have investigated robust and nonrobust aspects of AMOC variability and its mechanisms in a single coupled modeling framework, namely that of the CESM. For this purpose, we have performed a set of 600-yr-long

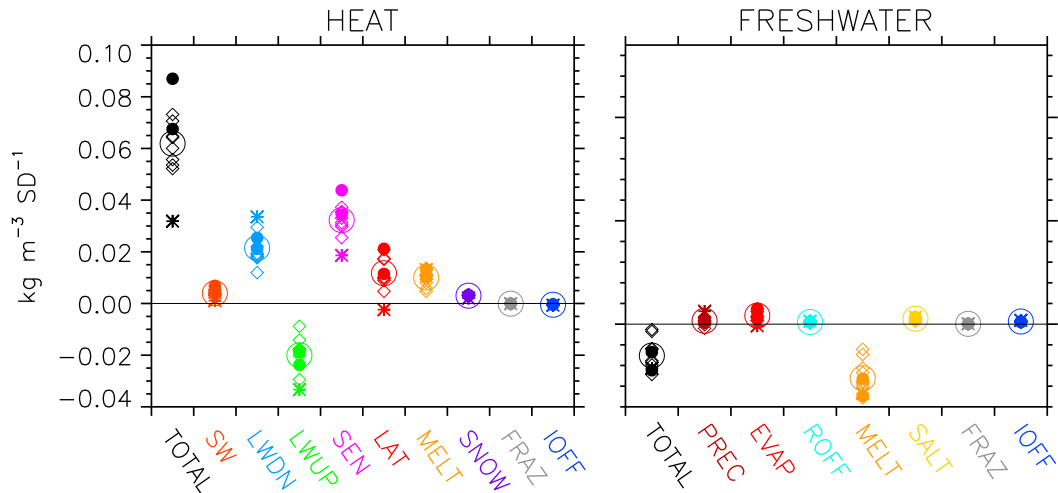


FIG. 11. As in Fig. 10, except that the (left) heat and (right) freshwater surface flux components are regressed onto the NAO time series and that the regressions are for lags  $-5$  to  $0$  with respect to the NAO time series. The unit is  $\text{kg m}^{-3}$  per unit index.

simulations for preindustrial conditions in which a few loosely constrained ocean model parameter values were changed within acceptable ranges with respect to a control simulation. These experiments were complemented by a pair of simulations where round-off perturbations were applied to the initial atmospheric temperature field and by a 2200-yr-long simulation of which the last 1800 years were used.

Two prominent nonrobust features of AMOC variability concern its temporal behavior. First, based on the individual reference red noise spectra, the time scales of variability differ among the cases, with the dominant periods ranging from decadal to multidecadal to even centennial. Indeed, in one of the cases (SUBM), the multidecadal period is very prominent, distinguishing this case from a few of the other cases. Second, these dominant periods are not stationary in time, varying considerably during the length of the simulations. In particular, in the LE suit of simulations, the dominant periods change from multidecadal to order centennial throughout the integration.

Although not necessarily surprising, these results are rather unsettling. Disparity in the dominant time scales among the CESM simulations is certainly quite large. While not well understood, we think that the factors that may impact these time scales include differences in stochastic NAO-related forcings, their timing and duration as well as seemingly subtle differences in the strength and spatial extent of the SPG, LS BLD, model mean states, advection, and deep western boundary current path (e.g., [Kwon and Frankignoul 2012, 2014](#); [Buckley and Marshall 2016](#)). The nonstationarity is consistent with what has been reported in a CCSM3 control simulation where a 300-yr-long very regular oscillatory regime with a period of 21 years was followed by a much weaker red noise–like irregular variability with a broad range of periods peaking at about 40 years ([Danabasoglu 2008](#); [Kwon and Frankignoul 2012](#)). This result indicates that robust characterization of AMOC variability requires multimillennium-scale simulations, but even such long runs may not be necessarily enough given the prominent nonstationarity depicted in the LE series of simulations. In other words, AMOC temporal variability may simply be nonstationary and nonrobust. Our results are reminiscent of [Wittenberg \(2009\)](#), where it is shown that long simulations are also needed to robustly characterize variability of El Niño, which has shorter dominant time scales than considered in our study. An implication here is that robust determination of impacts of parameterization changes on AMOC variability cannot be done in  $O(600)$ -yr simulations. Unfortunately, due to computational resource limitations, longer simulations are not routinely

performed by many modeling groups. Consequently, any definite statements about AMOC variability time scales from shorter simulations should be treated with caution.

Identification of dominant spectral peaks with respect to individual reference red noise spectra is common practice in AMOC variability studies. Such studies usually document variability in one individual model simulation. Our analysis here suggests that comparative statements about dominant variability periods across models could be misleading due to large sampling uncertainties.

In contrast to temporal variability, the pattern of the dominant spatial variability mode is very robust across all the cases. It shows a single cell pattern, covering the entire Atlantic basin, and it corresponds to a general strengthening and deeper penetration of the NADW cell in its positive phase. Such a single cell pattern as the dominant spatial variability mode is also present in many other models as well as in other CESM (CCSM) versions (e.g., [Msadek and Frankignoul 2009](#); [Tulloch and Marshall 2012](#); [Danabasoglu et al. 2012b](#)). Another robust finding is that with the parameterized overflows in CESM, changes in AMOC lead those of overflow product waters by about 7 years in the ensemble mean. Although this result is a rather robust feature of the CESM simulations, it differs from studies that used other coupled models (e.g., [Hawkins and Sutton 2008](#)) in which the Nordic seas overflows lead changes in AMOC, likely due to artificially deepened passageways.

Regarding the lead–lag relationships between the AMOC index and the LS March-mean BLD, LS  $\rho_{uo}$ , and the wintertime NAO, a very robust finding is that in all the simulations, the latter time series lead the AMOC index by 2–3 years, suggesting a driving role for changes in model's DWF site in the LS region as positive  $\rho_{uo}$  anomalies lead to deeper BLDs. The largest (negative) correlations between AMOC and SPG occur at lag 0, indicating simultaneous strengthening of AMOC and SPG transports. This relationship is also robust across all the cases. These results are consistent with those from CCSM4 discussed in [Danabasoglu et al. \(2012b\)](#). We note that such a prominent role for the LS properties in AMOC variability may be due to excessive deep water production there as CESM is among the models with such a bias (in historical simulations) in comparison to observational estimates from very short records ([Li et al. 2019](#)).

While the existence of positive  $\rho_{uo}$  anomalies prior to an AMOC intensification is a robust feature, respective contributions of temperature  $\rho_T$  and salinity  $\rho_S$  to these density anomalies are nonrobust across the simulations. Specifically, although in eight of the cases  $\rho_T$  contributes

much more strongly than salinity, accounting for >72% of the  $\rho_{uo}$  anomaly,  $\rho_S$  is the dominant contributor in one of the cases (MDO), accounting for 67% of the corresponding density anomaly. In the remaining two cases, temperature and salinity contributions are more comparable to each other. Following an AMOC intensification, all the cases robustly show that negative  $\rho_T$  and positive  $\rho_S$  anomalies substantially compensate each other, resulting in small density anomalies. This compensation is primarily due to the advection of warm and salty waters into the LS region associated with increased AMOC and SPG transports.

A heat budget analysis for the LS region shows that temperature acts to increase density in all cases prior to an AMOC intensification. This is primarily due to surface heat loss that is only partially balanced by diffusive processes. The two largest contributions to negative surface heat flux anomalies come from the sensible and latent heat flux components. The accompanying salt budget analysis reveals that the salt contribution to density varies across the cases, taking both positive and negative values. This balance is primarily between positive contributions from the diffusion and negative contributions from the advection terms. The surface flux contributions can be of either sign with an ensemble mean of about zero. Regression of surface heat and freshwater flux components onto the wintertime NAO index shows that the sensible and latent heat flux components are strongly associated with the positive phase of the NAO, suggesting that the NAO-related surface heat fluxes play a significant role in AMOC variability in all the experiments. We also find that the parameterized mesoscale and submesoscale advection terms make nonnegligible contributions to the heat and freshwater budgets (not shown), consistent with the findings of Danabasoglu et al. (2012b). Interestingly, in SUBM where we explicitly modify the minimum length scale of mixed layer fronts in anticipation of increasing the influence of the submesoscale parameterization at high latitudes, the magnitudes of the contributions of this parameterization to the LS tracer budgets remain very similar to those of the other cases.

In our analysis, we chose to use the AMOC maximum transport at 45°N as our index, arguing that such a *high-latitude* index is connected much more strongly with variability in the northern North Atlantic than other index choices such as AMOC maximum transport at 26.5°N or the PC1 time series. As discussed in Yeager and Danabasoglu (2012), various indices can exhibit substantial differences in their depictions of AMOC variability within a given simulation, reflecting different dominant variability mechanisms at different latitudes (e.g., the prominence of wind-driven high-frequency

variability at 26.5°N). A wavelet analysis based on the AMOC PC1 time series (not shown) produces rather similar spectra for all the cases as in Fig. 3 with somewhat different amplitudes. Furthermore, using this same index, we find that many elements identified as robust for the AMOC maximum transport at 45°N index remain so (not shown). An exception is that the relative contributions of  $\rho_T$  and  $\rho_S$  to the total  $\rho_{uo}$  change again, increasing the contributions of salinity. This further bolsters our conclusion that the relative contributions of  $\rho_T$  and  $\rho_S$  are nonrobust.

We use AMOC in latitude–depth space in our study. This choice is consistent with our goal of identifying robust and nonrobust aspects of AMOC variability as this depiction of AMOC is the most common framework that has been adopted in the literature. Such a depth-space representation emphasizes changes and variability in the deep southward (equatorward) circulation after DWF in the northern high latitudes (Kwon and Frankignoul 2014), consistent with our present focus. The density-space AMOC highlights upper-ocean changes within the SPG. Depending on the model, and perhaps the experiment, it can stress either northward or equatorward propagation of anomalies, showing a nonrobust behavior (Kwon and Frankignoul 2014; Zhang 2010). We think that both frameworks for studying AMOC and its variability are similarly model and experiment dependent, but both can be used in complementary ways to improve our understanding of AMOC variability and mechanisms.

Our results clearly show that, even in a single modeling framework, temporal variability characteristics of AMOC along with whether the DWF-region density anomalies are created by temperature or salinity contributions are nonrobust aspects of the model representation of AMOC. However, we take comfort in some robust features that include the pattern of the dominant spatial variability, a leading role for the positive upper-ocean density and boundary layer depth anomalies prior to an AMOC intensification, and the compensating temperature and salinity anomalies afterward. Finally, we also find a robust leading role for the NAO in influencing AMOC variability, strongly supporting the importance of NAO+-related buoyancy fluxes in the prevailing low-frequency variability mechanism.

*Acknowledgments.* This research was supported by the National Science Foundation (NSF) Collaborative Research EaSM2 Grant OCE-1243015 and by the National Oceanic and Atmospheric Administration (NOAA) Climate Program Office (CPO) under Climate Variability and Predictability (CVP) Program Grant NA13OAR4310138. It is also partially supported

by the NOAA CPO under CVP Program Grant NA16OAR4310170 and the Regional and Global Climate Modeling Program (RGCM) of the U.S. Department of Energy's (DOE) Office of Science (BER) through support of the HiLAT project. This material is based upon work supported by the National Center for Atmospheric Research (NCAR), which is a major facility sponsored by the NSF under Cooperative Agreement 1852977. The CESM project is supported by the NSF and the DOE Office of Science (BER). Computing resources were provided by the Climate Simulation Laboratory at NCAR's Computational and Information Systems Laboratory (CISL). We thank three anonymous reviewers for their constructive comments and suggestions.

## REFERENCES

- Abernathy, R., and J. C. Marshall, 2013: Global surface eddy diffusivities derived from satellite altimetry. *J. Geophys. Res. Oceans*, **118**, 901–916, <https://doi.org/10.1002/jgrc.20066>.
- Bates, M., R. Tulloch, J. Marshall, and R. Ferrari, 2014: Rationalizing the spatial distribution of mesoscale eddy diffusivity in terms of mixing length theory. *J. Phys. Oceanogr.*, **44**, 1523–1540, <https://doi.org/10.1175/JPO-D-13-0130.1>.
- Bellucci, A., A. Mariotti, and S. Gualdi, 2017: The role of forcings in the twentieth-century North Atlantic multidecadal variability: The 1940–75 North Atlantic cooling case study. *J. Climate*, **30**, 7317–7337, <https://doi.org/10.1175/JCLI-D-16-0301.1>.
- Bentsen, M., H. Drange, T. Furevik, and T. Zhou, 2004: Simulated variability of the Atlantic meridional overturning circulation. *Climate Dyn.*, **22**, 701–720, <https://doi.org/10.1007/s00382-004-0397-x>.
- Bjastoch, A., C. W. Böning, J. Getzlaff, J.-M. Molines, and G. Madec, 2008: Causes of interannual–decadal variability in the meridional overturning circulation of the mid-latitude North Atlantic Ocean. *J. Climate*, **21**, 6599–6615, <https://doi.org/10.1175/2008JCLI2404.1>.
- Booth, B. B., N. J. Dunstone, P. R. Halloran, T. Andrews, and N. Bellouin, 2012: Aerosols implicated as a prime driver of twentieth-century North Atlantic climate variability. *Nature*, **484**, 228–232, <https://doi.org/10.1038/nature10946>.
- Briegleb, B. P., G. Danabasoglu, and W. G. Large, 2010: An overflow parameterization for the ocean component of the Community Climate System Model. NCAR Tech. Note NCAR/TN-481+STR, 72 pp.
- Bryan, F. O., G. Danabasoglu, N. Nakashiki, Y. Yoshida, D. H. Kim, J. Tsutsui, and S. C. Doney, 2006: Response of North Atlantic thermohaline circulation and ventilation to increasing carbon dioxide in CCSM3. *J. Climate*, **19**, 2382–2397, <https://doi.org/10.1175/JCLI3757.1>.
- Buckley, M. W., and J. Marshall, 2016: Observations, inferences, and mechanisms of Atlantic meridional overturning circulation variability: A review. *Rev. Geophys.*, **54**, 5–63, <https://doi.org/10.1002/2015RG000493>.
- Cane, M. A., A. C. Clement, L. N. Murphy, and K. Bellomo, 2017: Low-pass filtering, heat flux, and Atlantic multidecadal variability. *J. Climate*, **30**, 7529–7553, <https://doi.org/10.1175/JCLI-D-16-0810.1>.
- Clement, A., K. Bellomo, L. N. Murphy, M. A. Cane, T. Mauritsen, G. Rädcl, and B. Stevens, 2015: The Atlantic Multidecadal Oscillation without a role for ocean circulation. *Science*, **350**, 320–324, <https://doi.org/10.1126/science.aab3980>.
- Cole, S. T., C. Wortham, E. Kunze, and W. B. Owens, 2015: Eddy stirring and horizontal diffusivity from Argo float observations: Geographic and depth variability. *Geophys. Res. Lett.*, **42**, 3989–3997, <https://doi.org/10.1002/2015GL063827>.
- Danabasoglu, G., 2008: On multidecadal variability of the Atlantic meridional overturning circulation in the Community Climate System Model version 3. *J. Climate*, **21**, 5524–5544, <https://doi.org/10.1175/2008JCLI2019.1>.
- , and J. C. McWilliams, 1995: Sensitivity of the global ocean circulation to parameterizations of mesoscale tracer transports. *J. Climate*, **8**, 2967–2987, [https://doi.org/10.1175/1520-0442\(1995\)008<2967:SOTGOC>2.0.CO;2](https://doi.org/10.1175/1520-0442(1995)008<2967:SOTGOC>2.0.CO;2).
- , and J. Marshall, 2007: Effects of vertical variations of thickness diffusivity in an ocean general circulation model. *Ocean Modell.*, **18**, 122–141, <https://doi.org/10.1016/j.ocemod.2007.03.006>.
- , W. G. Large, J. J. Tribbia, P. R. Gent, B. P. Briegleb, and J. C. McWilliams, 2006: Diurnal coupling in the tropical oceans of CCSM3. *J. Climate*, **19**, 2347–2365, <https://doi.org/10.1175/JCLI3739.1>.
- , R. Ferrari, and J. C. McWilliams, 2008: Sensitivity of an ocean general circulation model to a parameterization of near-surface eddy fluxes. *J. Climate*, **21**, 1192–1208, <https://doi.org/10.1175/2007JCLI1508.1>.
- , W. G. Large, and B. P. Briegleb, 2010: Climate impacts of parameterized Nordic Sea overflows. *J. Geophys. Res.*, **115**, C11005, <https://doi.org/10.1029/2010JC006243>.
- , S. C. Bates, B. P. Briegleb, S. R. Jayne, M. Jochum, W. G. Large, S. Peacock, and S. G. Yeager, 2012a: The CCSM4 ocean component. *J. Climate*, **25**, 1361–1389, <https://doi.org/10.1175/JCLI-D-11-00091.1>.
- , S. G. Yeager, Y.-O. Kwon, J. J. Tribbia, A. S. Phillips, and J. W. Hurrell, 2012b: Variability of the Atlantic meridional overturning circulation in CCSM4. *J. Climate*, **25**, 5153–5172, <https://doi.org/10.1175/JCLI-D-11-00463.1>.
- , and Coauthors, 2014: North Atlantic simulations in Coordinated Ocean-ice Reference Experiments phase II (CORE-II). Part I: Mean states. *Ocean Modell.*, **73**, 76–107, <https://doi.org/10.1016/j.ocemod.2013.10.005>.
- , and Coauthors, 2016: North Atlantic simulations in Coordinated Ocean-ice Reference Experiments phase II (CORE-II). Part II: Inter-annual to decadal variability. *Ocean Modell.*, **97**, 65–90, <https://doi.org/10.1016/j.ocemod.2015.11.007>.
- Delworth, T. L., and M. E. Mann, 2000: Observed and simulated multidecadal variability in the Northern Hemisphere. *Climate Dyn.*, **16**, 661–676, <https://doi.org/10.1007/s003820000075>.
- , and F. Zeng, 2016: The impact of the North Atlantic Oscillation on climate through its influence on the Atlantic meridional overturning circulation. *J. Climate*, **29**, 941–962, <https://doi.org/10.1175/JCLI-D-15-0396.1>.
- Duchon, C. E., 1979: Lanczos filtering in one and two dimensions. *J. Appl. Meteor.*, **18**, 1016–1022, [https://doi.org/10.1175/1520-0450\(1979\)018<1016:LFOAT>2.0.CO;2](https://doi.org/10.1175/1520-0450(1979)018<1016:LFOAT>2.0.CO;2).
- Eden, C., and J. Willebrand, 2001: Mechanism of interannual to decadal variability of the North Atlantic circulation. *J. Climate*, **14**, 2266–2280, [https://doi.org/10.1175/1520-0442\(2001\)014<2266:MOITDV>2.0.CO;2](https://doi.org/10.1175/1520-0442(2001)014<2266:MOITDV>2.0.CO;2).
- Enfield, D. B., A. M. Mestas-Nunez, and P. J. Trimble, 2001: The Atlantic multidecadal oscillation and its relationship to

- rainfall and river flows in the continental U.S. *Geophys. Res. Lett.*, **28**, 2077–2080, <https://doi.org/10.1029/2000GL012745>.
- Eyring, V., S. Bony, G. A. Meehl, C. A. Senior, B. Stevens, R. J. Stouffer, and K. E. Taylor, 2016: Overview of the Coupled Model Intercomparison Project phase 6 (CMIP6) experimental design and organization. *Geosci. Model Dev.*, **9**, 1937–1958, <https://doi.org/10.5194/gmd-9-1937-2016>.
- Ferrari, R., J. C. McWilliams, V. M. Canuto, and M. Dubovikov, 2008: Parameterization of eddy fluxes near oceanic boundaries. *J. Climate*, **21**, 2770–2789, <https://doi.org/10.1175/2007JCLI1510.1>.
- Ferreira, D., J. Marshall, and P. Heimbach, 2005: Estimating eddy stresses by fitting dynamics to observations using a residual-mean ocean circulation model and its adjoint. *J. Phys. Oceanogr.*, **35**, 1891–1910, <https://doi.org/10.1175/JPO2785.1>.
- Fox-Kemper, B., R. Ferrari, and R. Hallberg, 2008: Parameterization of mixed layer eddies. Part I: Theory and diagnosis. *J. Phys. Oceanogr.*, **38**, 1145–1165, <https://doi.org/10.1175/2007JPO3792.1>.
- , and Coauthors, 2011: Parameterization of mixed layer eddies. Part III: Implementation and impact in global ocean climate simulations. *Ocean Modell.*, **39**, 61–78, <https://doi.org/10.1016/j.oceomod.2010.09.002>.
- Frajka-Williams, E., and Coauthors, 2019: Atlantic meridional overturning circulation: Observed transport and variability. *Front. Mar. Sci.*, **6**, 260, <https://doi.org/10.3389/FMARS.2019.00260>.
- Gent, P. R., and J. C. McWilliams, 1990: Isopycnal mixing in ocean circulation models. *J. Phys. Oceanogr.*, **20**, 150–155, [https://doi.org/10.1175/1520-0485\(1990\)020<0150:IMIOCM>2.0.CO;2](https://doi.org/10.1175/1520-0485(1990)020<0150:IMIOCM>2.0.CO;2).
- , and Coauthors, 2011: The Community Climate System Model version 4. *J. Climate*, **24**, 4973–4991, <https://doi.org/10.1175/2011JCLI4083.1>.
- Hawkins, E., and R. Sutton, 2008: Potential predictability of rapid changes in the Atlantic meridional overturning circulation. *Geophys. Res. Lett.*, **35**, L11603, <https://doi.org/10.1029/2008GL034059>.
- Holland, M. M., D. A. Bailey, B. P. Briegleb, B. Light, and E. Hunke, 2012: Improved sea ice shortwave radiation physics in CCSM4: The impact of melt ponds and aerosols on Arctic sea ice. *J. Climate*, **25**, 1413–1430, <https://doi.org/10.1175/JCLI-D-11-00078.1>.
- Hurrell, J. W., and Coauthors, 2013: The Community Earth System Model: A framework for collaborative research. *Bull. Amer. Meteor. Soc.*, **94**, 1339–1360, <https://doi.org/10.1175/BAMS-D-12-00121.1>.
- Johns, W. E., and Coauthors, 2011: Continuous, array-based estimates of Atlantic Ocean heat transport at 26.5°N. *J. Climate*, **24**, 2429–2449, <https://doi.org/10.1175/2010JCLI3997.1>.
- Jungclauss, J. H., H. Haak, M. Latif, and U. Mikolajewicz, 2005: Arctic–North Atlantic interactions and multidecadal variability of the meridional overturning circulation. *J. Climate*, **18**, 4013–4031, <https://doi.org/10.1175/JCLI3462.1>.
- Karspeck, A. R., and Coauthors, 2017: Comparison of the Atlantic meridional overturning circulation between 1960 and 2007 in six ocean reanalysis products. *Climate Dyn.*, **49**, 957–982, <https://doi.org/10.1007/s00382-015-2787-7>.
- Kay, J. E., and Coauthors, 2015: The Community Earth System Model (CESM) Large Ensemble project: A community resource for studying climate change in the presence of internal climate variability. *Bull. Amer. Meteor. Soc.*, **96**, 1333–1349, <https://doi.org/10.1175/BAMS-D-13-00255.1>.
- Klavans, J. M., A. C. Clement, and M. A. Cane, 2019: Variable external forcing obscures the weak relationship between the NAO and North Atlantic multi-decadal SST variability. *J. Climate*, **32**, 3847–3864, <https://doi.org/10.1175/JCLI-D-18-0409.1>.
- Kwon, Y.-O., and C. Frankignoul, 2012: Stochastically-driven multidecadal variability of the Atlantic meridional overturning circulation in CCSM3. *Climate Dyn.*, **38**, 859–876, <https://doi.org/10.1007/s00382-011-1040-2>.
- , and —, 2014: Mechanisms of multidecadal Atlantic meridional overturning circulation variability diagnosed in depth versus density space. *J. Climate*, **27**, 9359–9376, <https://doi.org/10.1175/JCLI-D-14-00228.1>.
- Large, W. G., J. C. McWilliams, and S. C. Doney, 1994: Oceanic vertical mixing: A review and a model with a nonlocal boundary layer parameterization. *Rev. Geophys.*, **32**, 363–403, <https://doi.org/10.1029/94RG01872>.
- , G. Danabasoglu, J. C. McWilliams, P. R. Gent, and F. O. Bryan, 2001: Equatorial circulation in a global ocean climate model with anisotropic horizontal viscosity. *J. Phys. Oceanogr.*, **31**, 518–536, [https://doi.org/10.1175/1520-0485\(2001\)031<0518:ECOAGO>2.0.CO;2](https://doi.org/10.1175/1520-0485(2001)031<0518:ECOAGO>2.0.CO;2).
- Lawrence, D. M., K. W. Oleson, M. G. Flanner, C. G. Fletcher, P. J. Lawrence, S. Levis, S. C. Swenson, and G. B. Bonan, 2012: The CCSM4 land simulation, 1850–2005: Assessment of surface climate and new capabilities. *J. Climate*, **25**, 2240–2260, <https://doi.org/10.1175/JCLI-D-11-00103.1>.
- Li, F., M. S. Lozier, G. Danabasoglu, N. P. Holliday, Y.-O. Kwon, A. Romanou, S. G. Yeager, and R. Zhang, 2019: Local and downstream relationships between Labrador Sea Water volume and North Atlantic meridional overturning circulation variability. *J. Climate*, **32**, 3883–3898, <https://doi.org/10.1175/JCLI-D-18-0735.1>.
- Liu, Z., 2012: Dynamics of interdecadal climate variability: A historical perspective. *J. Climate*, **25**, 1963–1995, <https://doi.org/10.1175/2011JCLI3980.1>.
- Lozier, M. S., and Coauthors, 2019: A sea change in our view of overturning in the subpolar North Atlantic. *Science*, **363**, 516–521, <https://doi.org/10.1126/science.aau6592>.
- MacKinnon, J. A., and Coauthors, 2017: Climate process team on internal wave-driven ocean mixing. *Bull. Amer. Meteor. Soc.*, **98**, 2429–2454, <https://doi.org/10.1175/BAMS-D-16-0030.1>.
- Msadek, R., and C. Frankignoul, 2009: Atlantic multidecadal oceanic variability and its influence on the atmosphere in a climate model. *Climate Dyn.*, **33**, 45–62, <https://doi.org/10.1007/s00382-008-0452-0>.
- , K. W. Dixon, T. L. Delworth, and W. Hurlin, 2010: Assessing the predictability of the Atlantic meridional overturning circulation and associated fingerprints. *Geophys. Res. Lett.*, **37**, L19608, <https://doi.org/10.1029/2010GL044517>.
- , W. E. Johns, S. G. Yeager, G. Danabasoglu, T. L. Delworth, and A. Rosati, 2013: The Atlantic meridional heat transport at 26.5°N and its relationship with the MOC in the RAPID array and the GFDL and NCAR coupled models. *J. Climate*, **26**, 4335–4356, <https://doi.org/10.1175/JCLI-D-12-00081.1>.
- Murphy, L. N., K. Bellomo, M. Cane, and A. Clement, 2017: The role of historical forcings in simulating the observed Atlantic multidecadal oscillation. *Geophys. Res. Lett.*, **44**, 2472–2480, <https://doi.org/10.1002/2016GL071337>.
- Neale, R. B., and Coauthors, 2012: Description of the NCAR Community Atmosphere Model (CAM5.0). NCAR Tech. Note NCAR/TN-486+STR, 274 pp.
- Pickart, R. S., and M. A. Spall, 2007: Impact of Labrador Sea convection on the North Atlantic meridional overturning

- circulation. *J. Phys. Oceanogr.*, **37**, 2207–2227, <https://doi.org/10.1175/JPO3178.1>.
- Schlesinger, M. E., and N. Ramankutty, 1994: An oscillation in the global climate system of period 65–70 years. *Nature*, **367**, 723–726, <https://doi.org/10.1038/367723a0>.
- Smith, R. D., and Coauthors, 2010: The Parallel Ocean Program (POP) reference manual, ocean component of the Community Climate System Model (CCSM). Los Alamos National Laboratory Tech. Rep. LAUR-10-01853, 141 pp., <http://www.cesm.ucar.edu/models/cesm1.0/pop2/doc/sci/POPRefManual.pdf>.
- Sutton, R. T., G. D. McCarthy, J. Robson, B. Sinha, A. T. Archibald, and L. J. Gray, 2018: Atlantic multidecadal variability and the U.K. ACSIS program. *Bull. Amer. Meteor. Soc.*, **99**, 415–425, <https://doi.org/10.1175/BAMS-D-16-0266.1>.
- Tulloch, R., and J. Marshall, 2012: Exploring mechanisms of variability and predictability of Atlantic meridional overturning circulation in two coupled climate models. *J. Climate*, **25**, 4067–4080, <https://doi.org/10.1175/JCLI-D-11-00460.1>.
- Waterhouse, A. F., and Coauthors, 2014: Global patterns of diapycnal mixing from measurements of the turbulent dissipation rate. *J. Phys. Oceanogr.*, **44**, 1854–1872, <https://doi.org/10.1175/JPO-D-13-0104.1>.
- Wittenberg, A. T., 2009: Are historical records sufficient to constrain ENSO simulations? *Geophys. Res. Lett.*, **36**, L12702, <https://doi.org/10.1029/2009GL038710>.
- Xu, X., P. B. Rhines, and E. P. Chassignet, 2016: Temperature–salinity structure of the North Atlantic circulation and associated heat and freshwater transports. *J. Climate*, **29**, 7723–7742, <https://doi.org/10.1175/JCLI-D-15-0798.1>.
- , E. P. Chassignet, and F. Wang, 2019: On the variability of the Atlantic meridional overturning circulation transports in coupled CMIP5 simulations. *Climate Dyn.*, **52**, 6511–6531, <https://doi.org/10.1007/S00382-018-4529-0>.
- Yeager, S. G., and G. Danabasoglu, 2012: Sensitivity of Atlantic meridional overturning circulation variability to parameterized Nordic Sea overflows in CCSM4. *J. Climate*, **25**, 2077–2103, <https://doi.org/10.1175/JCLI-D-11-00149.1>.
- , and —, 2014: The origins of late-twentieth-century variations in the large-scale North Atlantic circulation. *J. Climate*, **27**, 3222–3247, <https://doi.org/10.1175/JCLI-D-13-00125.1>.
- Zhang, L., and C. Wang, 2013: Multidecadal North Atlantic sea surface temperature and Atlantic meridional overturning circulation variability in CMIP5 historical simulations. *J. Geophys. Res. Oceans*, **118**, 5772–5791, <https://doi.org/10.1002/jgrc.20390>.
- Zhang, R., 2010: Latitudinal dependence of Atlantic meridional overturning circulation AMOC variations. *Geophys. Res. Lett.*, **37**, L16703, <https://doi.org/10.1029/2010GL044474>.
- , R. Sutton, G. Danabasoglu, Y.-O. Kwon, R. Marsh, S. G. Yeager, D. E. Amrhein, and C. M. Little, 2019: A review of the role of Atlantic meridional overturning circulation in Atlantic multidecadal variability and associated climate impacts. *Rev. Geophys.*, **57**, 316–375, <https://doi.org/10.1029/2019RG000644>.